The Oceanic Response to Large-Scale Atmospheric Disturbances

J. WILLEBRAND,[1] S. G. H. PHILANDER AND R. C. PACANOWSKI

Geophysical Fluid Dynamics Laboratory/NOAA, Princeton University, Princeton, NJ 08540

(Manuscript received 24 April 1979, in final form 9 October 1979)

ABSTRACT

This paper is an analytical and numerical study of the response of the ocean to the fluctuating component of the wind stress as computed from twice-daily weather maps for the period 1973 to 1976. The results are described in terms of (time) mean and rms fields, frequency spectra and horizontal cross spectra, and local cross spectra between oceanic and atmospheric variables.

A forcing function with scales strictly larger than O(100 km) induces oceanic motion that is depth independent at periods between the inertial period and ~300 days. The dynamics is essentially linear so that rectified currents are small, the associated rectified transport amounts to at most 1–2 Sv in the western boundary layer. Root-mean-square currents are typically a few centimeters per second and are most intense in the western part of the basin, and near major topographic features. Fluctuations in the transport of the western boundary layer can be as large as 20–30 Sv. Three distinct frequency bands characterize the wind-induced barotropic fluctuations: 1) At periods between the inertial period and about one week the energy density increases steeply with decreasing frequency. Current spectra have a slope between −2 and −4. These forced waves can show an (imperfect) coherence between wind stress and the corresponding current components, and between atmospheric pressure and subsurface pressure. But spatial inhomogeneities in the wind field or bottom topography can destroy this coherence. 2) At periods between a week and a month planetary (or topographic) Rossby waves are dominant so that westward phase propagation is prominent. 3) At longer periods westward phase propagation is less evident and there is a time-dependent Sverdrup balance between meridional (cross-isobath) currents and wind stress curl. The spectra at these long periods are frequency independent (white) and the zonal (along-isobath) velocity component is more energetic than the meridional (cross-isobath) component.

Despite the high degree of idealization in the models, local coherence between oceanic and atmospheric variables is virtually nonexistent (except possibly at periods between 1 and 10 days) because of the wavelike structure of the oceanic response, the broadband stochastic character of the atmospheric variability, and inhomogeneities in the wind field and bottom topography.

It is proposed that fluctuations observed at site D north of the Gulf Stream are primarily atmospherically forced. At the MODE central mooring, however, there must be an additional energy source.

1. Introduction

The surface winds that drive the oceanic circulation have a fluctuating component with an rms amplitude which exceeds that of the mean winds over large regions. It is therefore important to know the nature of the oceanic variability induced by atmospheric disturbances. Previous studies of this variability concern the oceanic response to idealized atmospheric forcing functions such as sinusoidal wind fields and moving or standing disturbances (e.g., Longuet-Higgins, 1965; Pedlosky, 1965a; Phillips, 1966; Veronis, 1970; Philander, 1978; Leetma, 1978; Harrison, 1979). Gates (1968) studied the transient response to the sudden onset of steady winds. Magaard (1977) included the effect of buoyancy fluxes at the sea surface. Nearly all existing studies are deterministic and calculate the oceanic response to a particular wind field. The atmospheric variability, however, is more aptly described as a stochastic process, with a local correlation time (integral time scale) of a few days. The induced oceanic motions can therefore not be regarded as deterministic, and a description of atmospherically forced motion must explicitly take into account the broadband stochastic nature of both atmospheric and oceanic fields. Frankignoul and Müller (1979) have constructed a simplified stochastic forcing model, and calculated the spectral energy transfer to the ocean by a stationary and homogeneous wind field.

In order to go one step beyond the investigations mentioned above we have considered more realistic forcing fields by utilizing information from weather maps. Willebrand (1978) has analyzed twice-daily NMC sea surface pressure maps from 1973–76, and determined the spectral characteristics of the surface wind field over the ocean. This data set has several deficiencies, the most serious of which is the

[1] Present affiliation: Institut für Meereskunde an der Universität Kiel, 2300/Kiel, Germany.

0022-3670/80/030411-19$08.75

filtering of disturbances with scales much smaller than 1000 km. The data set, however, does describe the large-scale atmospheric disturbances accurately. Furthermore, better data are unlikely to be available in the near future. A study of the oceanic response to these winds therefore seems timely. In contrast to deterministic models, we regard our particular forcing as a realization of a random process. Accordingly, we have evaluated our results in terms of statistical parameters such as rms values and energy spectra. Ensemble averages have been replaced by time averages, although seasonal variations prevent the fields from being perfectly ergodic.

The wind field can be divided into a mean and a fluctuating part. The mean wind field drives an oceanic circulation characterized by intense western (and possibly northern) boundary currents which usually are unstable. There have been numerous investigations of the oceanic variability induced by these instabilities [see Robinson (1977) for a review of these studies]. In order to focus attention on atmospherically forced variability in the oceans, we have studied the response of a subtropical and midlatitude ocean to the fluctuating winds only (which by definition have zero mean), so that mean currents can be caused only by the rectifying effect of nonlinearities. Thus, we do not consider the instability mechanism, and we also exclude interactions between atmospherically induced variability and strong mean currents.

Our approach is to consider a hierarchy of models which are progressively more realistic (and complicated). In Section 2 we show that at periods between 1 and 300 days, the response of nontropical oceans to large-scale forcing is essentially barotropic. Hence the simplest conceivable model is described by the linear vorticity equation for an ocean with a flat floor. If the atmospheric forcing is assumed to be homogeneous in space and stationary in time, then for a simple β-plane geometry, analytical solutions can readily be derived. This is done in Section 2. In Section 3 we describe slightly more realistic results from a nonlinear numerical model that takes into account the non-stationarity and the inhomogeneity of the wind field. The response of this model is interpreted in the light of the results of Section 2. The model of Section 4 is more realistic because variations in the topography of the ocean floor, as well as irregular coast lines, are taken into account.

The most complicated system of all, of course, is the real ocean. In Section 5 we discuss oceanic measurements in order to determine the relevance of our results to the ocean. Of course, there is an enormous gap between our most sophisticated model and the ocean. Some of the factors that are responsible for that gap, such as the absence of small-scale forcing and of oceanic stratification, are discussed in Section 6 where we also summarize our principal results.

2. Analytical results

a. A simplified model

The oceanic response to time-dependent forcing can either be trapped (vertically and horizontally) to the neighborhood of the region that is forced, or it can take the form of waves that propagate away from the region. We shall confine our attention to sub-inertial frequencies so that the only propagating waves are Rossby waves. For a flat-bottom ocean without lateral boundaries the shaded part of Fig. 1 shows for which frequencies and wavenumbers Rossby waves can be excited. (The highest frequency shown in Fig. 1 corresponds to the inertial frequency of 45° latitude.) For frequencies and wavenumbers in the unshaded region of Fig. 1 the response is trapped.

Since the horizontal scale of large atmospheric disturbances is comparable to the size of ocean basins, the horizontal trapping scale is not of much interest. The vertical trapping can be described by an equation of the type

$$\frac{\partial^2 W}{\partial z^2} - \left(k^2 + \frac{\beta k_1}{\omega}\right)\frac{N^2(z)}{f^2 - \omega^2} W = \text{forcing} \quad (1)$$

(see, e.g., Philander, 1978). Here W is the amplitude of a vertical eigenfunction, and $\mathbf{k} = (k_1, k_2)$ is horizontal wavenumber; otherwise the notation is standard. In the WKB approximation, the vertical trapping scale (e-folding distance) z_e is given implicitly by

$$\int_{-z_e}^{0} \left[\left(k^2 + \frac{\beta k_1}{\omega}\right)\frac{N^2(z)}{f^2 - \omega^2}\right]^{1/2} dz = 1. \quad (2)$$

This scale (km) is shown in the unshaded part of Fig. 1 for a typical midlatitude stratification $N(z) = N_0 \exp(z/b)$ with $N_0 = 7.3 \times 10^{-3}$ s^{-1} and $b = 1.3$ km (cf. Garrett and Munk, 1972).

The oceanic response can be strongly trapped near the ocean surface when the atmospheric disturbances have scales smaller than 100 km, or when their periods are longer than a few hundred days or are close to the inertial period. When these conditions are not met the trapped response penetrates to the ocean floor and is depth independent, i.e., barotropic. In the shaded part of Fig. 1 where Rossby waves are excited, the response is baroclinic only at periods $>$ 300 days which is off our scale. (That is the shortest period for a first baroclinic mode Rossby wave at 45°N, with the same stratification parameters as above.) The two lines shown in the shaded area are dispersion lines for barotropic Rossby waves for two values of the meridional wavenumber k_2.

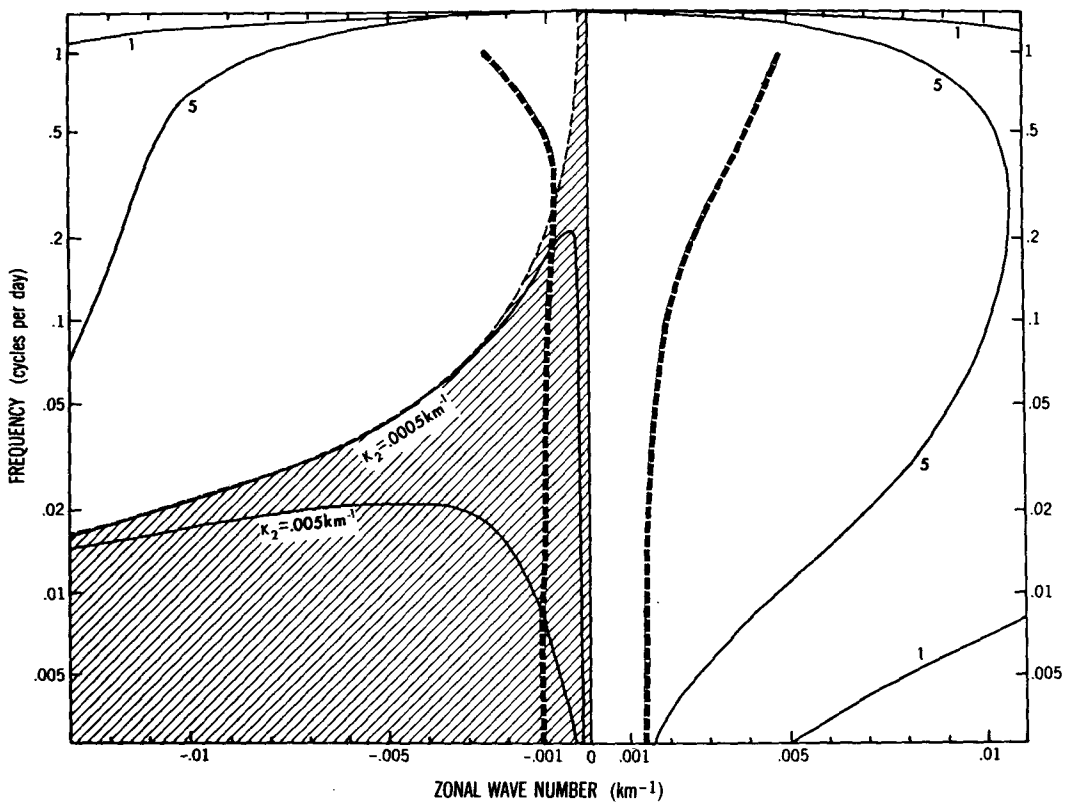

FIG. 1. A dispersion diagram. Rossby waves are excited in the shaded area where dispersion lines are drawn for two values of the meridional wavenumber k_2. In the unshaded area the response decays exponentially from the forcing region (the surface). Lines that correspond to e-folding depths of 1 and 5 km are shown. 95% of the variance of atmospheric disturbances falls between the heavy dashed lines.

The location of the atmospheric energy in frequency-wavenumber space is indicated by the two heavy dashed lines in Fig. 1. The lines are taken from Willebrand's (1978) analysis of synoptic weather maps and are defined such that for each frequency ~95% of the variance of atmospheric pressure fluctuations fall within these curves. It is, then, clear that at periods between 1 and 300 days the oceanic response to large-scale forcing is essentially barotropic, in agreement with results by Veronis and Stommel (1956) and Phillips (1966). However, that conclusion is based on atmospheric data which are heavily smoothed in space, thus truncating small-scale variability. The effects of high-wavenumber atmospheric forcing are discussed below (cf. Section 6).

The barotropic response of the ocean is described by the vertically averaged equations of motion. In the quasi-geostrophic limit, one can define a transport streamfunction $\psi(\mathbf{x},t)$ and derive the (inviscid) vorticity equation on a β-plane

$$\left(\nabla^2 - \frac{f^2}{gH}\right)\frac{\partial \psi}{\partial t} + J[\psi,\nabla^2\psi] + HJ[\psi,f/H] = F. \quad (3)$$

Here J denotes the Jacobian, and F the forcing function. The horizontal velocity components u_1 and u_2 and the surface elevation ζ are related to ψ as

$$u_1 = -\frac{1}{H}\frac{\partial \psi}{\partial x_2}, \quad u_2 = \frac{1}{H}\frac{\partial \psi}{\partial x_1}, \quad \zeta = \frac{f\psi}{gH} - \frac{P_a}{g}. \quad (4)$$

Eq. (3) is an approximation to conservation of potential vorticity and holds for sufficiently small bottom slopes. For the remaining part of this section, we will furthermore neglect the influence of topographic variations altogether. We will also neglect the nonlinear terms in (3), because in the range of scales considered here the Rossby number is typically $O(10^{-3})$. This approximation will be supported later by the results of the nonlinear numerical model.

With these simplifications, (3) takes the familiar form

$$\left(\nabla^2 - \frac{f^2}{gH}\right)\frac{\partial \psi}{\partial t} + \beta\frac{\partial \psi}{\partial x_1} = F. \quad (5)$$

The atmospheric forcing can be caused by wind stress, pressure fluctuations or buoyancy fluxes at the surface. It is worthwhile noting that the latter type of forcing is not in conflict with our assumption

of barotropic motion. As demonstrated by Magaard (1977), all three mechanisms generate a vertical velocity field at the bottom of a (frictional or diffusive) upper layer. Whether or not the induced motion is baroclinic only depends on the *scale* of that velocity field, not on its origin. We did, however, not investigate the influence of buoyancy fluxes further because good buoyancy flux data were not at hand and explicit modeling of the diffusive boundary layer is required for this type of forcing.

With respect to wind stress and air pressure, the forcing function takes the simple form

$$F = \mathrm{curl}_z \boldsymbol{\tau} - \frac{f}{g}\frac{\partial P_a}{\partial t}. \tag{6}$$

Here $\boldsymbol{\tau}$ and P_a denote kinematic wind stress and air pressure, respectively. For the time being, we will neglect the forcing due to air pressure in (6). Its relative importance compared to wind stress forcing is discussed below.

A scale analysis of Eq. (5) reveals that there exists a time-scale $T = L\beta^{-1}[L^{-2} + (f^2/gH)]$ such that

(i) $t \ll T$—the β-effect is negligible and only forced waves are possible;
(ii) $t \sim T$—the β-effect is important and Rossby waves are possible;
(iii) $t \gg T$—explicit time dependence is negligible and a Sverdrup balance obtains.

For a horizontal length scale L of ~1000 km, $T \approx 0.7$ day corresponding to a period of 4–5 days. Accurate solutions will, in fact, show that the appropriate value of that period is somewhat longer, around 10 days. Why this is so can be inferred from Fig. 1. Although Rossby waves are in principle possible anywhere in the shaded area of Fig. 1, the finite dimensions of an ocean basin limit the horizontal wavelengths and, because of the dispersion relation, also limit the possible periods of Rossby waves. If the size of the basin is 5000 km, Rossby waves are possible only at periods $\geq$ 10 days. Hence at periods < 10 days the response is in the form of forced waves (whose structure could be affected by the β-effect). The size of the ocean basin also puts a lower limit on the frequency range for long Rossby waves. There are, however, other reasons why, below a certain frequency, one is likely to find a Sverdrup balance rather than propagating Rossby waves.

In the interior of the ocean, far from the coasts, the linear response to steady winds is a Sverdrup balance. If the winds had suddenly started to blow at one instant, then a finite time would have elapsed before the establishment of a Sverdrup balance. Lighthill (1969) showed that this time is equal to the time it takes a long non-dispersive Rossby wave to propagate, from the eastern coast, to the point under consideration.

Short Rossby waves are also excited at the western coast of the ocean basin but these play no role in the establishment of the Sverdrup balance. They are simply superimposed on that balance. In the case of time-dependent winds one expects a Sverdrup balance on time scales long compared to the time it takes a long non-dispersive Rossby wave to propagate across the ocean basin from the eastern boundary. If the horizontal scale of the waves coincides with that of the basin and is L, then this time is T, as given before. On time scales comparable to T the oceanic response will still appear to be in the form of Rossby waves because the short waves with eastward group velocities are present. As the period increases, the wavelengths of these waves decrease so that they become prone to dissipation. Hence on time scales long compared to T these short waves are unlikely to be observed and a Sverdrup balance will be obtained. In summary the response of the ocean at high frequencies—periods up to 10 days or so—will be in the form of forced waves: at periods between 10 days and about 30 days Rossby waves will be excited, and at longer periods there is likely to be a Sverdrup balance.

b. *Spectra of the response*

As argued in the Introduction, it is useful to consider both the atmospheric forcing and the oceanic response as essentially random variables. Hence, instead of looking at deterministic solutions to (5) we shall try to understand the response in terms of statistical parameters such as spectra and cross correlations. We will at first assume that the fluctuations are statistically stationary in time and homogeneous in space. Although these assumptions are far from being accurate (see Fig. 3 below), they will enable us to understand qualitatively most results of the more complex numerical model.

For a Fourier-component $\hat{\psi}(\mathbf{k},\omega)\exp[i(\mathbf{k}\cdot\mathbf{x} - \omega t)]$, Eq. (5) can be written

$$iD(\mathbf{k},\omega)\hat{\psi}(\mathbf{k},\omega) = \hat{F}(\mathbf{k},\omega), \tag{7}$$

where

$$D(\mathbf{k},\omega) = \omega(k^2 + f^2/gH) + \beta k_1 \tag{7a}$$

and $\mathbf{k} = (k_1,k_2)$ is the horizontal wavenumber vector.

It would be an easy task to include dissipation, e.g., in the form of a linear bottom friction law, in (5) and the subsequent discussion. In the Rossby-wave regime the magnitude of the fluctuating current critically depends on the amount of friction (see, e.g., Harrison, 1979). However, because of the large phase speed of Rossby waves the effect of lateral boundaries cannot be neglected. We defer discussion of the resonant case to the next section, and consider the off-resonant case $D(\mathbf{k},\omega) \neq 0$ where supposedly both friction and lateral boundaries play a minor role. From (7) we can calculate energy

spectra of the oceanic variables in terms of the frequency-wavenumber spectrum

$$E_F(\mathbf{k},\omega) = \langle \hat{F}^*(\mathbf{k},\omega)\hat{F}(\mathbf{k},\omega)\rangle/2\Delta\mathbf{k}\Delta\omega$$

of the atmosphering forcing (wind stress curl) which can be obtained from the cross spectra of the wind stress components τ_1 and τ_2 as

$$E_F(\mathbf{k},\omega) = k_1^2 E_{\tau_2}(\mathbf{k},\omega) + k_2^2 E_{\tau_1}(\mathbf{k},\omega) - 2k_1k_2\,\mathrm{Re}[A_{\tau_1\tau_2}(\mathbf{k},\omega)]. \quad (8)$$

Frequency spectra of streamfunction and currents are then given by

$$E_\psi(\omega) = \int d\mathbf{k} E_F(\mathbf{k},\omega)/D^2(\mathbf{k},\omega),$$

$$\left.\begin{matrix} E_{u_1}(\omega) \\ E_{u_2}(\omega) \end{matrix}\right\} = \int d\mathbf{k} \left\{\begin{matrix} k_2^2 \\ k_1^2 \end{matrix}\right\} E_F(\mathbf{k},\omega)/D^2(\mathbf{k},\omega). \quad (9)$$

For time scales much shorter than 10 days, the planetary effects associated with the β-term in $D(\mathbf{k},\omega)$ will become small. Furthermore, if we neglect the effects of divergence, then $D(\mathbf{k},\omega) = \omega k^2$. It follows that the current spectra are given by

$$\left.\begin{matrix} E_{u_1}(\omega) \\ E_{u_2}(\omega) \end{matrix}\right\} = \omega^{-2} \int d\mathbf{k} \left\{\begin{matrix} k_2^2 \\ k_1^2 \end{matrix}\right\} E_F(\mathbf{k},\omega) k^{-4}. \quad (10)$$

Twice the total kinetic energy per frequency band is given by

$$E_{u_1}(\omega) + E_{u_2}(\omega) = \omega^{-2} E_F(\omega)\overline{k^{-2}}, \quad (11)$$

where

$$\overline{k^{-2}} = \frac{\int E_F(\mathbf{k},\omega)k^{-2}d\mathbf{k}}{\int E_F(\mathbf{k},\omega)d\mathbf{k}}, \quad (12)$$

and $E_F(\omega) = \int E_F(\mathbf{k},\omega)d\mathbf{k}$ is the frequency spectrum of wind stress curl.

To proceed further, one has to know the frequency-wavenumber spectrum of the wind field. We will utilize the following general properties of the wind spectra (for reference see Willebrand, 1978; Frankignoul and Müller, 1979):

(i) The frequency spectrum of wind stress curl is almost constant (white) for $\omega < \omega_0$, where $\omega_0 \approx 2\pi/3$ days corresponds to the dominant time scale of synoptic activity (i.e., eastward traveling cyclones.

(ii) At periods shorter than 3 days the spectrum falls off as $\omega^{-\alpha}$ where $\alpha \approx 1.5$.

(iii) The horizontal scale of atmospheric disturbances is constant at low frequencies but decreases at frequency above 0.1 cpd. Hence the quantity k^{-2} in (12) will be a decreasing function of frequency. (Generally, we expect $\overline{k^{-2}}$ to behave like $\overline{k^{2}}^{-1}$ although for broadband wavenumber spectra the magnitude of both quantities may be somewhat different.)

(iv) The wind field is *symmetric* with respect to horizontal wavenumber at frequencies $\omega < \omega_0$. At higher frequencies, the wind fluctuations have a preferred propagation direction, which is strongly eastward with a small northward component.

It now follows from (11) that the kinetic energy spectrum of the oceanic response will follow a power law $\omega^{-\beta}$ with $\beta \geq 2$ in the 3–10 days range and $\beta \geq 3.5$ in the 1–3 days range.

At very low frequencies ($\omega < 2\pi/50\ d$) the time derivative in (5) becomes small, and the response to fluctuating forcing is essentially a time-dependent Sverdrup balance. For this case $D(\mathbf{k},\omega) = \beta k_1$ and we obtain from (5)

$$\left.\begin{matrix} E_{u_1}(\omega) \\ E_{u_2}(\omega) \end{matrix}\right\} = \beta^{-2} \left\{\begin{matrix} \overline{(k_2/k_1)^2} \\ 1 \end{matrix}\right\} E_F(\omega) \quad (13)$$

Since the curl spectrum is white at low frequencies, the same will be true of the oceanic current spectra. The magnitude of $\overline{(k_2/k_1)^2}$ depends on the details of the directional structure of the forcing spectrum. In general we expect $\overline{(k_2/k_1)^2} \gg 1$, and in the case of an isotropic forcing spectrum it will be infinitely large. Physically, this is so because isotropic forcing includes the point $k_1 = 0$ which falls on resonance curves as $\omega \to 0$. (Geostrophic zonal currents satisfy the unforced equations of motion and therefore are resonant.) For a spectrum $E_F(\mathbf{k},\omega) = (k_1k_2)^2\phi(k,\omega)$, which is one of the most simple non-isotropic forms avoiding the resonance problem, one obtains $\overline{(k_2/k_1)^2} = 3$. Hence at low frequencies we expect the zonal kinetic energy to be greater than the meridional kinetic energy. We also expect both their spectra to be white.

Thus far we have discussed the high-frequency band (period < 10 days) and the low-frequency band (period > 30 days) where $D \neq 0$. In the intermediate frequency range where Rossby waves are excited, resonant basin modes are possible especially in a basin with a simple closed geometry). Hence large peaks will occur in the spectra, their magnitude being determined by frictional effects which so far have been neglected. For a rectangular basin with east-west dimensions L_1, and north-south dimensions L_2, the resonance frequencies are given by

$$\omega_{mn} = \frac{\beta}{2}\left[\left(\frac{m\pi}{L_1}\right)^2 + \left(\frac{n\pi}{L_2}\right)^2 + \frac{f^2}{gH}\right]^{-1/2}, \quad m, n = 1, 2, \ldots. \quad (14)$$

The corresponding solution to (5) without forcing is given by

$$\psi_{mn} \approx \exp(i\omega_{mn}t - i\beta x/2\omega_{mn}) \sin(m\pi x/L_1) \times \sin(n\pi y/L_2). \quad (15)$$

Theoretically, there is a resonant mode associated with each integer combination (m,n). However, whether or not these modes are established depends on the relative magnitude of two characteristic times: the time T_{prop} it takes a Rossby wave to propagate across the basin, and the lifetime T_{diss} of a wave as determined by dissipation. The ratio of these two time scales, based on east-west group velocities for Rossby waves, and on the friction law as used in Eq. (21) below, is

$$\frac{T_{\text{diss}}}{T_{\text{prop}}} = \frac{\beta|k_1^2 - k_2^2 - f^2/gH|}{2A_H L_1 k^2 (k^2 + f^2/gH)^2} \quad (16)$$

For parameter values typical of oceanic conditions one finds that $T_{\text{diss}} \lesssim T_{\text{prop}}$ for the short eastward traveling waves for which $k_1^2 \gg k_2^2$, and also for a small range of wavenumbers in the neighborhood of $k_1^2 = k_2^2 + f^2/gH$. Only if $T_{\text{diss}} \gg T_{\text{prop}}$ can waves cross the basin many times during their lifetime and possibly establish basin modes. It follows that only a finite (and possibly small) number of resonant modes is likely to be established.

c. *Coherence between oceanic and atmospheric fluctuations*

In the light of the results described above, spectra of oceanic variables can be inspected to determine the relevance of these ideas to the ocean. However, very different phenomena can give rise to the same spectra so that more stringent tests for the importance of wind forcing are desirable. In particular, one can look for coherence between the oceanic and atmospheric variability. In the frequency range where propagating Rossby waves are important, there is no reason to expect any coherence between oceanic motion observed at one point, and the local atmospheric variability. In this frequency range we should look for Rossby wave characteristics such as westward phase propagation. Outside the Rossby wave range, the oceanic motion is locally forced by the atmosphere, and one might expect a resemblance between the oceanic and atmospheric variability. We will investigate this question in terms of the local cross spectra between oceanic and atmospheric variables.

From Eqs. (4) to (6) we obtain for the velocity Fourier components

$$\left.\begin{aligned} \hat{u}_1(\mathbf{k},\omega) &= \frac{i}{D}(k_2^2\hat{\tau}_1 - k_1k_2\hat{\tau}_2) \\ \hat{u}_2(\mathbf{k},\omega) &= \frac{i}{D}(k_1^2\hat{\tau}_2 - k_1k_2\hat{\tau}_1) \end{aligned}\right\}. \quad (17)$$

The cross spectra between current and wind stress components are defined as

$$A_{u_\alpha\tau_\beta}(\omega) = \int d\mathbf{k}\langle \hat{u}_\alpha^*(\mathbf{k},\omega)\hat{\tau}_\beta(k,\boldsymbol{\omega})\rangle = \int d\mathbf{k} A_{u_\alpha\tau_\beta}(\mathbf{k},\omega). \quad (18)$$

From (17) it follows then that

$$A_{u_1\tau_1}(\omega) = i\int d\mathbf{k}[k_2^2 E_{\tau_1}(\mathbf{k},\omega) - k_1k_2A_{\tau_2\tau_1}(\mathbf{k},\omega)]/D, \quad (19a)$$

$$A_{u_1\tau_2}(\omega) = i\int d\mathbf{k}[k_2^2 A_{\tau_1\tau_2}(\mathbf{k},\omega) - k_1k_2E_{\tau_2}(\mathbf{k},\omega)]/D, \quad (19b)$$

$$A_{u_2\tau_1}(\omega) = i\int d\mathbf{k}[k_1^2 A_{\tau_2\tau_1}(\mathbf{k},\omega) - k_1k_2E_{\tau_1}(\mathbf{k},\omega)]/D, \quad (19c)$$

$$A_{u_2\tau_2}(\omega) = i\int d\mathbf{k}[k_1^2 E_{\tau_2}(\mathbf{k},\omega) - k_1k_2A_{\tau_1\tau_2}(\mathbf{k},\omega)]/D. \quad (19d)$$

To evaluate (19), we again have to know the wavenumber structure of the wind stress field in detail. Nevertheless, some qualitative conclusions are possible, provided we use an observational property of the wind spectra, namely, their near symmetry with respect to north-south wavenumber. The symmetry implies that $E_{\tau_\alpha}(\mathbf{k},\omega)$ is an even, and $A_{\tau_1\tau_2}(\mathbf{k},\omega)$ an odd function of the north-south wavenumber k_2. (It also implies that $A_{\tau_1\tau_2}(\omega) = \int dk\, A_{\tau_1\tau_2}(\mathbf{k},\omega) = 0$ which is in accordance with the observed low coherence between wind stress components.) Hence, the integrands in (19b,c) are odd functions of k_2 so that $A_{u_1\tau_2}(\omega) = A_{u_2\tau_1}(\omega) = 0$. On the other hand, the integrands in (19a,c) are even functions of k_2. At high frequencies where $D = \omega k^2$, the integrands should be essentially real and positive, and we expect $u_1 - \tau_1$ and $u_2 - \tau_2$ to be correlated but to be 90° out of phase. It is obvious that any divergent contribution to the wind stress field must lower the correlation as only the wind stress curl is forcing in Eq. (5).

In the Sverdrup regime, the wind fluctuations are symmetric in k_1. Because $D \approx \beta k_1$, the integrands will be antisymmetric in k_1 and we expect no strong correspondence between any current and stress components. We do expect coherence between the meridional velocity component u_2 and the curl of the wind stress. Furthermore, as wind stress curl and atmospheric pressure are normally well correlated (at least if computed from synoptic maps), we also expect a somewhat lower coherence between u_2 and P_a, with a phase difference of 180°.

3. The response of a numerical model

In order to take the effects of coasts and topography into account, in order to allow for possible nonlinear effects and in order to permit a spatially inhomogeneous and non-stationary forcing function, it is necessary to obtain solutions numerically. The model we use should be viewed as a refined version of the one discussed in Section 2. We shall therefore determine the extent to which the results obtained in that section apply to a slightly more realistic (but still very idealized) situation.

a. The model

We initially used a multilevel baroclinic model with realistic stratification. As one would expect on the basis of the argument presented in Section 2, the response was found to be entirely depth-independent (except for a shallow Ekman layer at the surface) at periods between 1 and 200 days. We therefore proceeded with a two-dimensional barotropic model. This model was developed by Blumberg (1977) who gives details concerning the method of solution for the shallow water equations which in spherical coordinates read

$$\frac{\partial U_1}{\partial t} + \mathcal{L}_A U_1 - \frac{U_1 U_2 \tan\theta}{ah} - fU_2 + \frac{gh}{a\cos\theta}\frac{\partial \zeta}{\partial \lambda} = X_1 + A_H\left(\mathcal{L}_D U_1 - \frac{2\sin\theta}{a^2\cos^2\theta}\frac{\partial u_2}{\partial \lambda}\right), \quad (20a)$$

$$\frac{\partial U_2}{\partial t} + \mathcal{L}_A U_2 + \frac{U_1^2 \tan\theta}{ah} + fU_1 + \frac{gh}{a}\frac{\partial \zeta}{\partial \theta} = X_2 + A_H\left(\mathcal{L}_D U_2 + \frac{2\sin\theta}{a^2\cos^2\theta}\frac{\partial u_1}{\partial \lambda}\right), \quad (20b)$$

$$\frac{\partial \zeta}{\partial t} + \frac{1}{a\cos\theta}\frac{\partial U_1}{\partial \lambda} + \frac{1}{a\cos\theta}\frac{\partial}{\partial \theta} U_2 \cos\theta = 0. \quad (20c)$$

Here $h = H + \zeta$ denotes the total depth of the ocean, $U_\alpha = u_\alpha h$ the total transport, θ latitude, λ longitude and a the radius of the earth. The horizontal advection and dissipation operators are defined as

$$\mathcal{L}_A = \frac{1}{a\cos\theta}\left(\frac{\partial}{\partial \lambda} u_1 + \frac{\partial}{\partial \theta} u_2 \cos\theta\right), \quad (21a)$$

$$\mathcal{L}_D = \frac{1}{a^2}\left(\frac{h}{\cos^2\theta}\frac{\partial^2}{\partial \lambda^2}\frac{1}{h} + \frac{h}{\cos\theta}\frac{\partial}{\partial \theta}\cos\theta\frac{\partial}{\partial \theta}\frac{1}{h} + 1 - \tan^2\theta\right). \quad (21b)$$

The results to be reported in this section were obtained for an idealized ocean basin of constant depth $H = 4$ km, resembling in size the North Atlantic with east-west walls along 25 and 60°N, and north-south walls along 0° and 80°W. The horizontal resolution was 1° in longitude and 0.7° in latitude so that there were 80 × 52 grid points. The friction parameter A_H was taken to be 5×10^7 cm^2 s^{-1}, this choice being motivated by requirements of computational stability. The sensitivity of the results to other values of A_H is discussed below.

The terms X_1 and X_2 in (20) represent the external forcing. For wind stress forcing, we have $(X_1, X_2) = (\tau_1, \tau_2)$. Numerical experiments which included an air pressure forcing term $(-H\nabla P_a)$ had almost identical results, except of course for a change in sea level which reacts as an inverse barometer. This result is in agreement with the findings of Frankignoul and Müller (1979) who demonstrated that air pressure forcing is generally small compared to wind stress forcing in the range of space-time scales considered here. The stress field in (20) was computed from twice-daily NMC weather maps from 1973–76; for details see Willebrand (1978).

The barotropic model (20) resolves surface gravity waves so that the appropriate time step in the finite-difference version of (20) is much smaller than for a quasi-geostrophic model. Most of our results could probably have been derived with a model that solves the barotropic vorticity equation (3). The principal reason for using the model (20) was its availability at the time we embarked on this study. A further comparison of primitive equation vs quasigeostrophic models can be found in Semtner and Holland (1978).

b. Gross features of the response

Fig. 2 shows the resulting distribution of the east (u_1) velocity field with longitude for a 6-month period in the first year of the simulation. The prominent feature is the tilt in the isopleths which indicates westward phase propagation practically everywhere, with phase velocities of the order 3–5 m s^{-1}. The particle velocity is typically a few centimeters per second and its amplitude increases from early summer to late fall. This increase is almost synchronous with a seasonal increase in amplitude of the wind stress fluctuations. One also can identify groups of wavetrains moving eastward from the western boundary with a speed up to 1 m s^{-1}. We conclude that planetary waves with westward phase propagation but possibly eastward group velocity constitute a dominant part of the response of our numerical model to fluctuating winds. In order to arrive at more quantitative conclusions, we now consider some statistical parameters of the oceanic response.

The time-mean value at each grid point was removed from the wind stress field in order to focus on

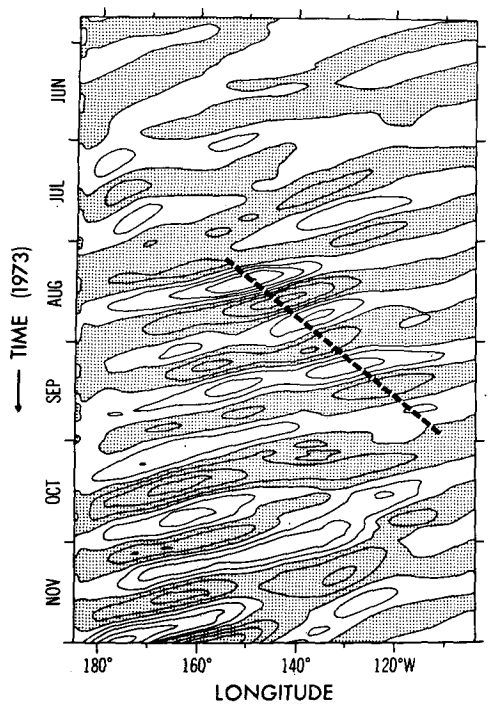

FIG. 2. A time-longitude plot of zonal velocity fluctuations in the numerical model along 42°N. Shaded regions indicate westward flow. The contour interval is 1.5 cm s^{-1}. The heavy dashed line corresponds to an eastward group velocity of 80 cm s^{-1}.

the oceanic response to purely fluctuating forcing. Hence, any *mean* current generated by those winds would indicate nonlinear rectification. In general, the mean currents in our model were very small, of the order 0.02 cm s^{-1}. Only near the western boundary magnitudes as large as 0.2 cm s^{-1} were found, extending over a longitudinal distance of ~200 km. That corresponds to a transport of 1–2 Sv, northward in the northern and southward in the southern part of the basin. While that signature is in agreement with previous investigations by Pedlosky (1965a) and Veronis (1970), the magnitude of these rectified currents is small compared, for example, to typical Gulf Stream transports. This conclusion is in variance with Veronis' (1970) statement that a fluctuating wind may generate a rectified circulation of up to 50% of the response to a steady wind of same amplitude.

There are two principal reasons for the unimportance of nonlinearities in our model:

(i) The low speeds and large horizontal scales of the oceanic motion cause the Rossby number to be very small, more than one order of magnitude smaller than the one used in Veronis' (1970) calculations. A similar difference in Rossby number exists between our numerical simulation and the tank experiments of Whitehead (1975) and Firing and Beardsley (1976) in which oscillating forcing on a β-plane equivalent generated rectified currents.

(ii) A second reason for the lack of rectification is the stochastic nature of the forcing. From (3) it can be demonstrated easily that fluctuations consisting of propagating waves with *random* phase relations do not induce a secondary circulation. Fixed phase relations can occur due to reflections at a lateral boundary when propagating waves form a basin mode, and also due to nonlinear interactions within the wave field. They could also be a consequence of an idealized non-random structure of the forcing field.

We emphasize again that our numerical results apply to *purely* fluctuating forcing only. The possibility remains that interactions of the waves with mean currents generated by the mean wind field could intensify the mean currents, particularly in the western boundary layer. Away from boundaries, however, it seems more likely that the energy transfer is in the opposite direction (Müller, 1978).

Maps of rms values for u_1, u_2 and ζ are shown in Fig. 3. Typical values are 3 cm s^{-1} for the horizontal velocity components and 20 cm for the surface elevation. Although the variability is caused by wind stress fluctuations, the rms maps do not resemble the rms stress distribution closely (cf. Fig. 3d), indicating that nonlocal processes (waves) must play a dominant role. Specifically, the accumulation of energy in the western part of the basin is characteristic of planetary waves, since those with an eastward group velocity travel much slower and have much smaller spatial scales than those with a westward group velocity (Pedlosky, 1965b). The field of surface elevation is smoother than that of the velocities. In quasigeostrophic motions ζ essentially is the streamfunction which is smoother (has larger scales) than its derivatives if the motion covers a broad band of spatial scales.

Fig. 4 displays frequency spectra from time series of u_1, u_2 and ζ at three points in the basin. The most conspicuous features are maxima in the energy density at periods near 10 and near 16 days. Since the wind spectra at those periods are rather smooth, these distinct frequencies must reflect a property of the oceanic model, and we tentatively ascribe them to resonant basin modes.

Toward higher frequencies the spectra fall off very rapidly, ultimately following a power law $\sim \omega^{-q}$ with q having a value between 3 and 4. (The spectral analysis was such that spectra as steep as $q = 8$ could have been estimated.) In this frequency range we expect wave propagation to be unimportant; the motion is likely to be forced locally.

At periods longer than about one month, most of the spectra flatten out and are more or less white

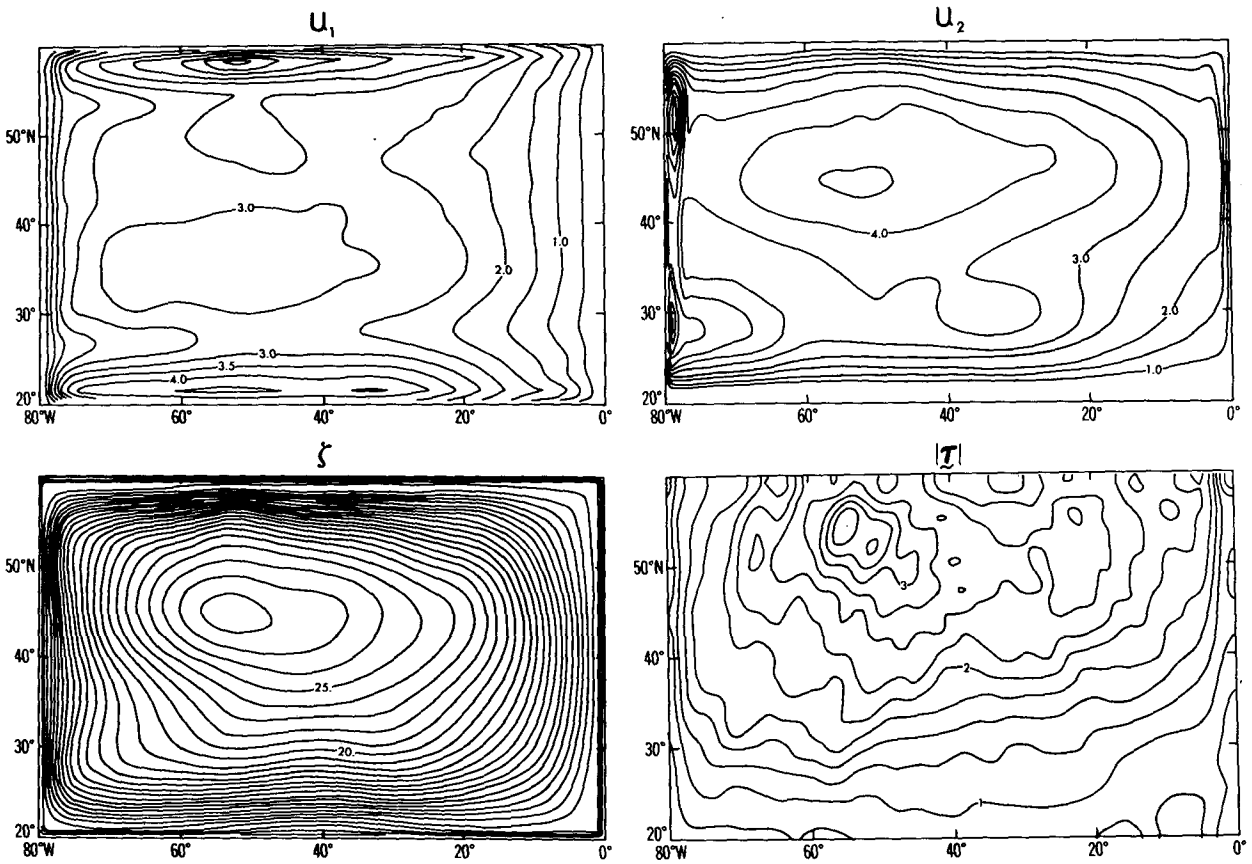

FIG. 3. Maps of the standard deviation (rms) of zonal (u_1) and meridional (u_2) velocity components (cm s^{-1}) of sea surface elevation ζ (cm) and of wind stress τ (dyn cm^{-2}).

within their statistical accuracy. For reasons given earlier, we expect the dynamics to be governed by a Sverdrup balance in this frequency range.

Fig. 5 displays coherences and phase differences of the three oceanic fields for an east-west (a) and north-south (b) separation. The coherences are nearly perfect in the basin mode regime, and have lower values both at higher and lower frequencies. In Fig. 5a the phases indicate westward propagation in the basin mode range. At lower frequencies the phases remain negative but return slowly to zero, indicating a gradual transition into the Sverd-

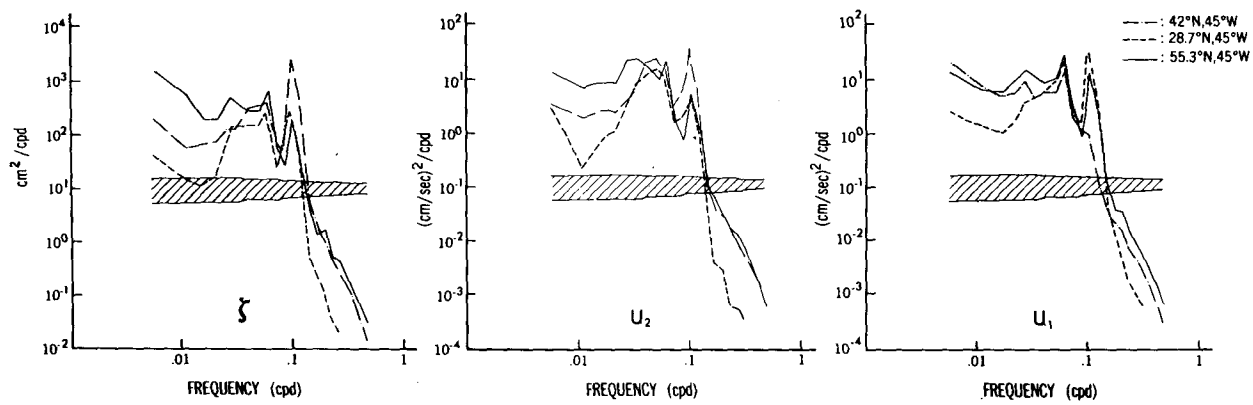

FIG. 4. Model spectra of oceanic variables (u_1,u_2,ζ) at latitudes 27.8°N, 42°N and 55.3°N along the meridian 45°W. Shaded area indicates 95% confidence limits.

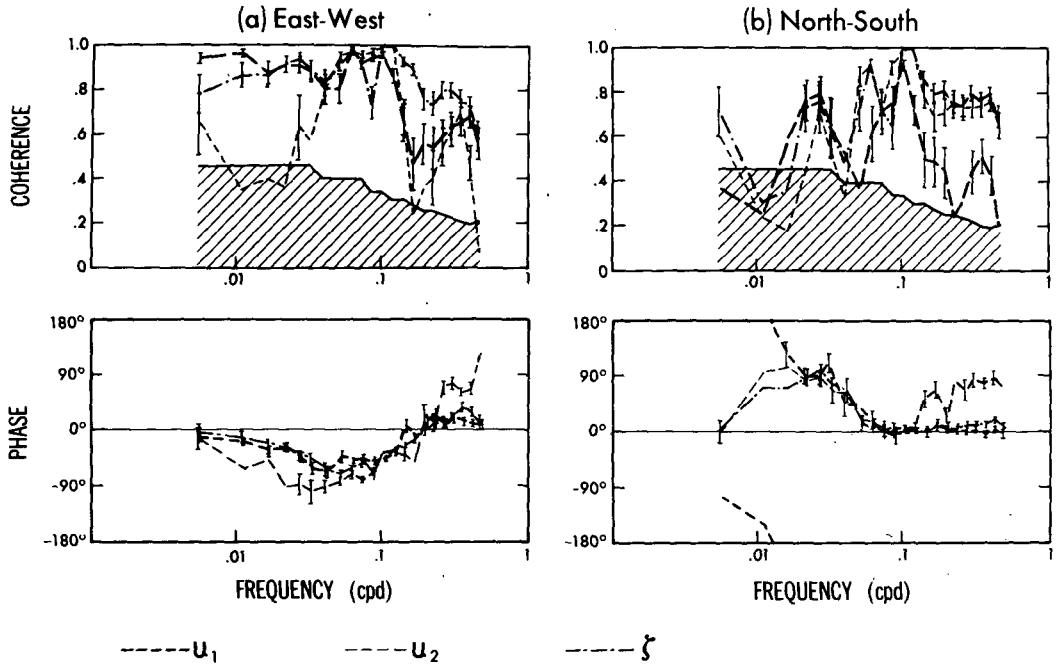

FIG. 5. Cross spectra of oceanic variables between two points (45°W and 39°W) along 42°N in (a) and between 42°N and 47.6°N along 45°W in (b). Positive phases indicate eastward (a) and northward (b) propagation of signals. Error bars indicate 95% confidence interval.

rup regime. Betwen 0.1 and 0.2 cpd, the phases become positive which corresponds to eastward propagation, in accordance with direct forcing by the atmosphere.

Next we discuss in detail each of the three frequency ranges identified here.

c. *Rossby waves*

Eq. (14) gives the frequencies at which the spectral peaks in Fig. 4 should occur. The numerical values are listed in Table 1 for values of L_1 and L_2 appropriate to our basin. Also listed is for each mode (or more precisely, for its constituent with eastward group velocity) is the ratio of dissipation to propagation time according to (16). That ratio exceeds unity for only five modes which are the most likely ones to be excited, and it decreases rapidly with increasing mode numbers.

TABLE 1. Periods $T_{mn} = 2\pi/\omega_{mn}$, according to Eq. (14) for $L_1 = 6550$ km and $L_2 = 3885$ km, and the ratio $T_{\text{diss}}/T_{\text{prop}}$, with $A_H = 5 \times 10^7$ cm^2 s^{-1}. The parameter $\beta = \partial f/\partial y$ is evaluated at 42.5°N.

m	n	T_{mn} (days)	$T_{\text{diss}}/T_{\text{prop}}$
1	1	9.1	11.8
2	1	11.6	4.9
3	1	14.8	1.9
4	1	18.4	0.8
1	2	15.1	1.2
2	2	16.7	1.0
3	2	19.0	0.6
1	3	21.6	0.2
2	3	22.8	0.3
3	3	24.6	0.2

It is obvious that the peaks near 10 days in Fig. 4 correspond to the gravest mode $m = n = 1$. The latitudinal structure agrees with that of the eigensolutions in (15), i.e., the fields of u_2 and ζ have maxima at the central latitude 42.5°N, while u_1 has a node here.

Ordering the modes according to their value $T_{\text{diss}}/T_{\text{prop}}$, we next expect a peak for $(m,n) = (2,1)$ which should occur around 11.6 days. However, inspection of (15) shows that for this oscillation the fields of u_1 and ζ have nodes at the central longitude where the spectra of Fig. 4 are evaluated. The field of u_2 does not have a mode, but a minimum of rms amplitude at this longitude.

The identification of the peak(s) around 16 days is more difficult as the candidates (3,1), (1,2) and (2,2) are rather close in period, and the frequency resolution of Fig. 4 is not sufficient to clearly distinguish between them. At the center point (curve a) (1,2) contributes to the peak in u_1, while (3,1) shows up in the spectra of u_2 and ζ. Off the center, both modes have nonzero amplitude, and additionally (2,2) can contribute to the spectra of u_2.

At lower frequencies, no further basin modes can

be identified clearly. Obviously, the slow speed of waves with eastward group velocity prevents the establishment of modes with higher wavenumbers. We nonetheless expect that down to some lower frequency the oceanic response is *locally* in the form of free waves satisfying the dispersion relation $D(\mathbf{k},\omega) = 0$. As a confirmation we note that the east-west phase differences in Figs. 5a–5c remain negative down to fairly low frequencies (~0.02 cpd) where a gradual transition into the Sverdrup regime takes place.

The non-vanishing phase differences in Fig. 5a are caused by east-west asymmetries, either of the oceanic model (at low frequencies) or the wind field (at high frequencies). While the latter also has a small tendency for northward propagation at high frequencies which shows up in Fig. 5b, we would expect north-south symmetry (and zero phases) at low frequencies, in contrast to the pronounced northward propagation observed in Fig. 5b. Most likely, this asymmetry is a consequence of the fact that the wind amplitude is largest in the northern part of the basin (cf. Fig. 3d) and the generation of waves is more effective here than it is in the southern part. Hence, at the basin center we expect to see an excess of waves with southward group velocity which corresponds to northward phase propagation. The amount of that excess depends, besides on the forcing field, on the strength of friction and is larger for short Rossby-waves than for the gravest basin modes.

d. The Sverdrup balance

In Section 2 we argued that at low frequencies a Sverdrup balance is likely so that

$$\beta H u_2 = \mathrm{curl}_z \boldsymbol{\tau}. \tag{22}$$

According to this equation, fluctuations of the meridional velocity should be coherent and in phase with fluctuations of wind stress curl. Another implication of (22) is a much higher level of zonal than meridional kinetic energy. [See the discussion following Eq. (13)]. This prediction is indeed borne out at low frequencies by the spectra in Fig. 4.

On the other hand, the model shows no correlation between u_2 and curl $\boldsymbol{\tau}$. Apparently, the presence of short Rossby waves, though they were not very energetic, can destroy the expected coherence. We therefore look for a non-local check of the Sverdrup balance. Eq. (22) implies that the net mass flux across a circle of latitude in the basin is equal to the integral of the curl of the wind stress along that latitude. This flux must be balanced by a northward transport in the western boundary layer. Fig. 6 shows the (low-pass filtered) transport variations in this boundary layer, and the low-pass filtered integral

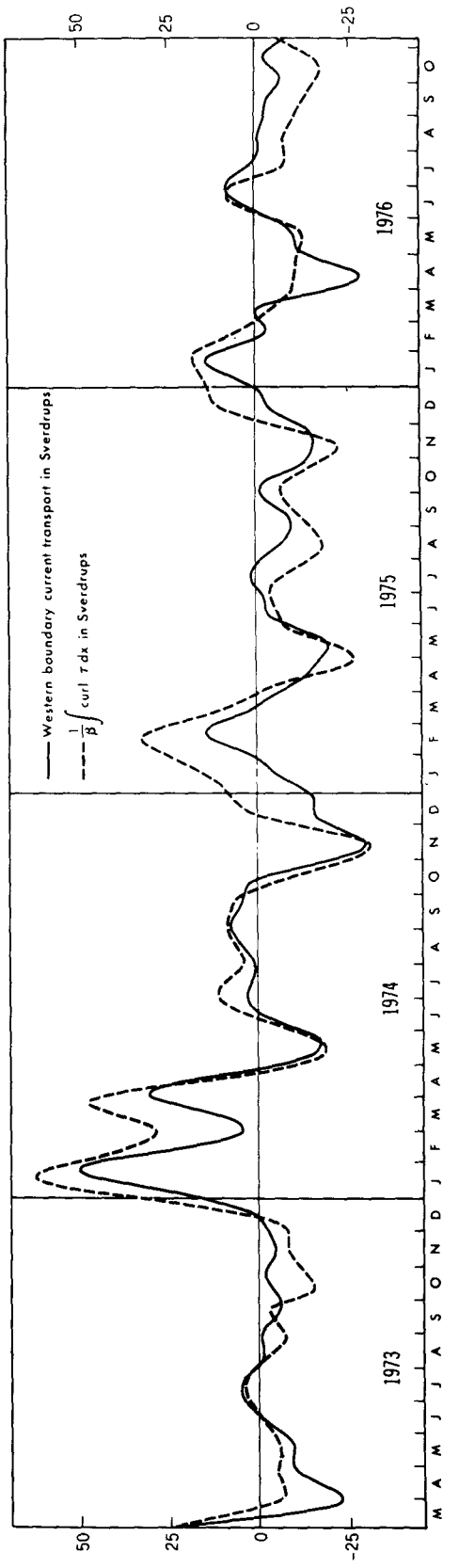

FIG. 6. Transport of the western boundary current (within a distance of 300 km of the western coast) across 40°N as a function of time. The transport as calculated from the curl of the wind stress by using the Sverdrup equation is also shown.

of $\text{curl}_z\ \tau$, both along 42°N. There clearly is a high correlation between the curves. Discrepancies can be ascribed to 1) the presence of short Rossby waves with eastward group velocity and 2) inadequate numerical resolution of the western boundary layer. As argued above, nonlinear effects are unlikely to cause significant deviations from the Sverdrup relation (22).

The salient feature of the transport and $\text{curl}_z\ \tau$ fluctuations in Fig. 6 is the unusual event of the winter of 1974–75. The absence of a pronounced seasonal cycle is striking. This is consistent with a linear oceanic response to a wind stress whose components do not have a pronounced seasonal cycle (Willebrand, 1978). If a western boundary current such as the Gulf Stream or Kuroshio current has seasonal fluctuations in midlatitudes then it must be due to a nonlinear response to the wind—the wind speed does have a strong seasonal cycle—or it must be due to the seasonal cycle in the tropics where the western boundary current originates.

e. *Forced high-frequency motion*

The steep spectral slopes of the frequency spectra in Fig. 4 in the period range from 1 to 10 days are in qualitative agreement with the simple analytical model of Section 2 [cf. Eq. (11) and following discussion]. Quantitative deviations result from the closeness of the inertial frequency on one end and the first basin mode on the other end of that period range. The eastward phases in Fig. 5a also confirm that model. As a further test, we consider the local correlations between oceanic and atmospheric fields (Fig. 7). No significant correlation exists in the wave regime and in the Sverdrup regime, whereas strong (though not perfect) coherence between $u_1 = \tau_1$, $u_2 - \tau_2$ and $\zeta - P_a$ exists at high frequencies. This result agrees well with the prediction of Eq. (19). The phases tend toward zero with increasing frequency, instead of remaining at 90° as predicted from (19). This tendency is due to leakage from the inertial frequency; it disappeared when that leakage was reduced by omitting prewhitening in the spectral analysis.

It is worthwhile noting that the results in Fig. 7 were obtained in a highly idealized situation. Any additional complication, such as more complicated geometry, topography, more complex numerical model, etc., is likely to reduce the few significant coherences even further.

The results in Fig. 7 are from the center of the basin where the wind field is reasonably homogeneous in space. (To put it differently, the scale of inhomogeneities exceeds the correlation scale there.)

This is not true everywhere in the basin. In particular, in the southwest corner of our basin near 20°N, which is in the transition region from prevailing easterlies to prevailing westerly winds, the scale of inhomogeneities in the wind field is small. In that region of our model we find no coherence between oceanic currents and wind stress components.

f. *The sensitivity to horizontal friction*

The preceding results are for a constant coefficient of eddy viscosity with a value of $5 \times 10^7\ \text{cm}^2\ \text{s}^{-1}$. Fig. 8 shows kinetic energy spectra, at a mid-ocean station, for this value of A_H and for the value $A_H = 1.5 \times 10^8$. It is evident that the spectra are significantly modified only at frequencies corresponding to those of the basin modes. The high-frequency forced waves are unaffected by a change in the value of A_H but at low frequencies energy levels are

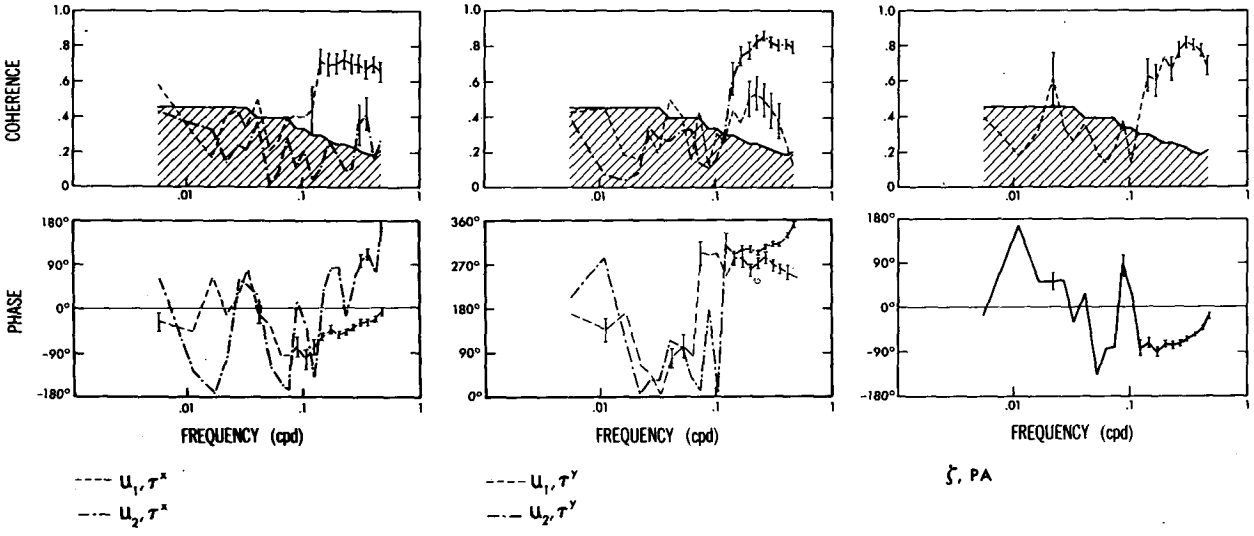

FIG. 7. Cross spectra between oceanic and atmospheric variables at (45°W, 42°N). Positive phase if oceanic variable leads atmospheric variable.

slightly lower when the value of A_H is increased. This probably is due to the dissipation of short Rossby waves (with eastward group velocities). Nevertheless, even with the larger of the two values (22) still is a good approximation to the Sverdrup regime.

We also have experimented with different types of friction in (20), namely, linear bottom friction and a biharmonic friction law. Except for some rather obvious differences resulting from the different damping rates of large and small scales, respectively, the overall structure of the oceanic response remained unchanged as to be expected in a system where friction is not a dominant mechanism.

In addition to studying the oceanic response to winds observed over the North Atlantic, we also studied the response of a Pacific Ocean model (whose size exceeds that of atmospheric cyclones), to the winds observed there. (Figs. 8 and 6 are actually from the Pacific calculation). Except for a slight change in resonant frequencies, the results were similar to the Atlantic results principally because the winds have similar structures.

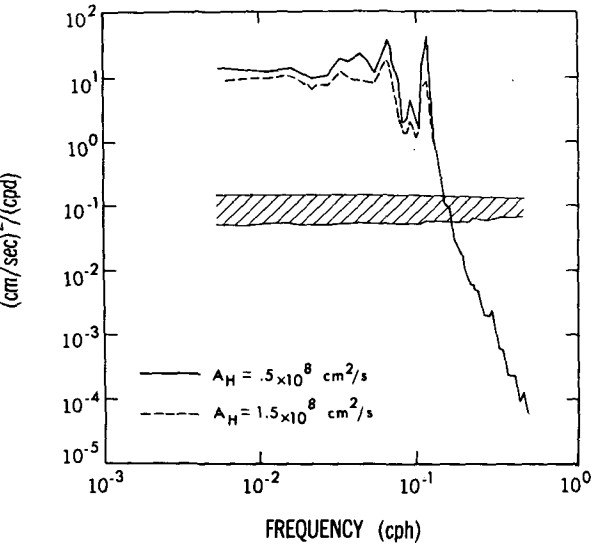

FIG. 8. Kinetic energy spectra from the center of the flat-bottomed ocean for different values of the coefficient of lateral friction.

4. The influence of topography

The oceanic response to large-scale forcing can differ strikingly from the results of the previous sections if the bottom topography of the ocean is taken into account. The presence of topography introduces a further length scale (or a spectrum of length scales), and the scales of forcing and response are no longer directly related. Especially the answer to the question whether or not the flow will be baroclinic now depends on the topographic as well as the atmospheric scale.

To be definite, let us assume that the atmospheric scale is much larger than that of topography. The wind-induced barotropic flow, as described in the previous sections, then produces a vertical velocity field at the bottom, which has the same scales as the topography. That vertical velocity can induce either an additional barotropic signal or a (bottom-trapped) baroclinic motion. Which of the two possibilities occurs, can be decided with the same arguments as were used to derive (2). The integration in (2) now has to start at the bottom, and hence for a given frequency-wavenumber combination the vertical trapping scale will somewhat exceed the one displayed in Fig. 1, because the oceanic stratification is much weaker near the bottom than it is near the surface.

However, the scale of the topography now replaces that of atmospheric forcing. More precisely, the *slope* of the topography is relevant as the kinematic boundary condition relates vertical velocity and bottom slope. Typically, at high wavenumbers the spectrum of topography is isotropic and $\sim k^{-2}$ (Bell, 1975) so that the slope spectrum is white. The bandwidth of a white spectrum (formally infinite) is determined by a cutoff wavenumber which corresponds to a scale of a few kilometers. It follows that the response to large-scale wind fields will have a small-scale, bottom-intensified baroclinic component (cf. McWilliams, 1974).

A barotropic model, however, can still be useful if one is interested only in scales of motion larger than those causing the baroclinic response, i.e., larger than O(100 km). If in Eq. (20) transport and elevation are interpreted as suitable horizontal averages, if the topography is sufficiently smooth, and if Reynolds stresses arising from the baroclinic motion are negligible, then (20) may still be used to determine the large-scale barotropic response in the presence of topography.

There have been several studies of the effect of topography on oceanic motion. See, for example, the analytical results of Rhines and Bretherton (1973), Thomson (1975) and Odulo and Pelinovsky (1978). Herring (1977) and Holloway (1978) employ techniques developed in turbulence theory to study this problem. Bretherton and Haidvogel (1976) adopt a numerical approach. The principal results for our purposes are the following:

1) Topography can support free waves with a frequency $\omega = 0(f\Delta H/H)$, where $\Delta H/H$ is the relative height of the bottom feature. This frequency is often higher than the frequency associated with planetary waves. Hence topography can cause the free and forced wave regions to overlap or it can cause the frequency band associated with forced waves to become very small. In either case identification of forced waves may be difficult.

2) If the flow is sufficiently nonlinear for two-dimensional turbulent cascades to be important then the steady velocity component parallel to bottom contours intensifies.

3) If the scale of spatial inhomogeneities of the topography is comparable to, or smaller than, the correlation scale of the motion, then the coherence that exists between different variables in the absence of topography, can be destroyed.

The numerical experiment of Section 3 was repeated but now we included the (smoothed) topography and shape of the North Atlantic Ocean. Fig. 9a shows the dynamically relevant f/H contours in the model. The mean (rectified) currents remained uninterestingly small; nonlinear interactions were apparently unimportant. The rms transport $[\overline{(u_1'H)^2} + \overline{(u_2'H)^2}]^{1/2}$ is shown in Fig. 9b. Compared to Fig. 3, this pattern is strongly topographically controlled. Large values occur principally near topographic features such as the mid-Atlantic ridge. The transport fluctuations are comparable in magnitude to those in the flat-bottom experiment. This implies that, despite the reduction in horizontal scale, the effects of lateral friction remain small (except at resonant frequencies).

Whereas the flat-bottom spectra in Fig. 4 are representative of a large region in the basin, spectra from the topographic case vary considerably over short distances. This is evident in Fig. 10 which shows frequency spectra of horizontal transport variations as a function of latitude and longitude. The most striking feature in Fig. 10a is the concentration of energy at a period of about 5 days in the neighborhood of 40°N, west of the Azores. These fluctuations are resonantly generated topographic waves which cannot propagate away from the bump. The less pronounced peak at a period of ~10 days, in the vicinity

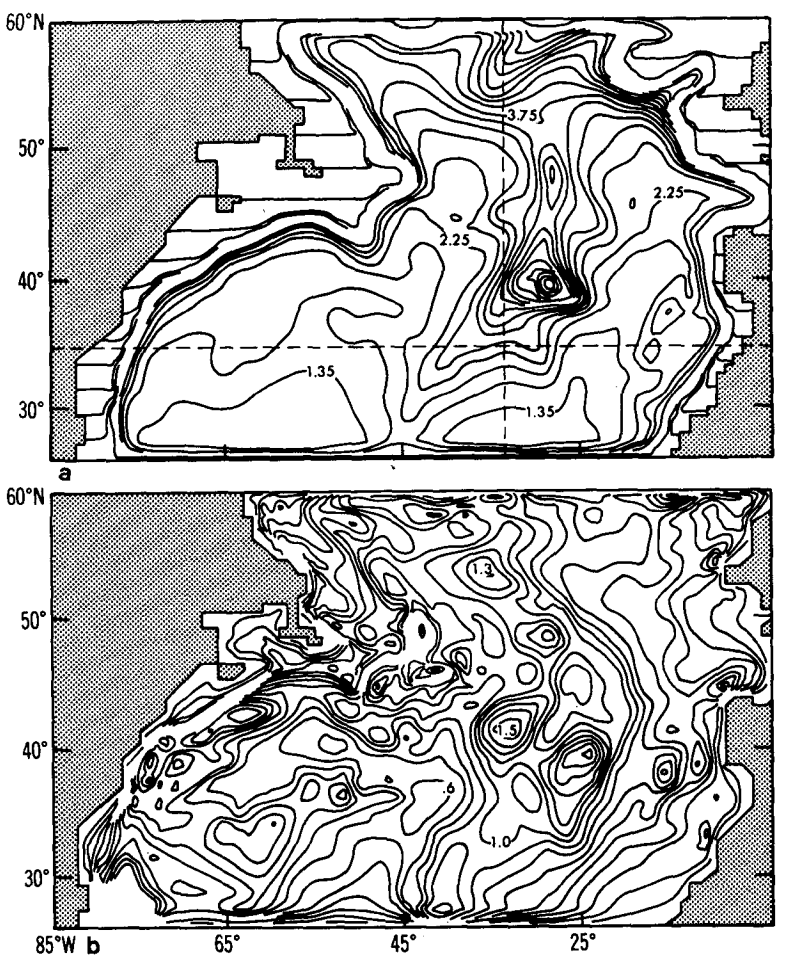

FIG. 9a. A map of f/h contours used in the model of Section 4. Values are in units of 10^{-10} cm^{-1} s^{-1}. The contour interval is 0.3×10^{-10} cm^{-1} s^{-1}. 9b. A map of the standard deviation of kinetic energy of the vertically integrated velocities. Isopleths are at intervals of 1×10^5 cm^{-2} s^{-1}. The units of the values shown are 10^6 cm^2 s^{-1}.

of 50°N, is likely to be a resonant topographic wave, too. Resonant waves with these periods are unlikely to be observed at these locations in the ocean because the wave properties are sensitive to the details of the topographic features, and there is only a crude resemblance between the topography in our model and that in the ocean. Hence the detailed structure of these resonant topographic waves is of little interest. What is important is that such waves can be excited by large-scale atmospheric disturbances. Taylor *et al.* (1977) appear to have observed resonant topographic waves around the Gillis Seamount in the western part of the North Atlantic.

Spectra for the section along 35°N show strong variability at periods between 25 and 50 days. This is probably due to the large number of f/H contours that intersect this section (see Fig. 9a). The generalized Sverdrup balance which replaces (22), and which is the linearized low-frequency limit of (3), reads

$$\mathbf{U} \cdot \frac{\partial(f/H)}{\partial \mathbf{x}} = H^{-1} \operatorname{curl}_z \boldsymbol{\tau}. \tag{23}$$

This equation relates the velocity normal to f/H contours to the local wind stress curl. The tangential velocity is found by integrating the continuity equation along a contour line. Hence there should be strong variability when crossing contours of very different shape.

At high frequencies the spectra are steep, at low frequencies the spectra are white, as in the flat-bottom case.

There was essentially no coherence between oceanic and atmospheric variables at any frequency, presumably because of the small scale of inhomogeneities associated with the topography.

A calculation for the geometry of Fig. 9a but with the depth constant (H = 4 km) yielded results practically identical to those described in Section 3. Irregular coast lines have a small effect on wind-induced velocity fluctuations compared to the effect of topographic features.

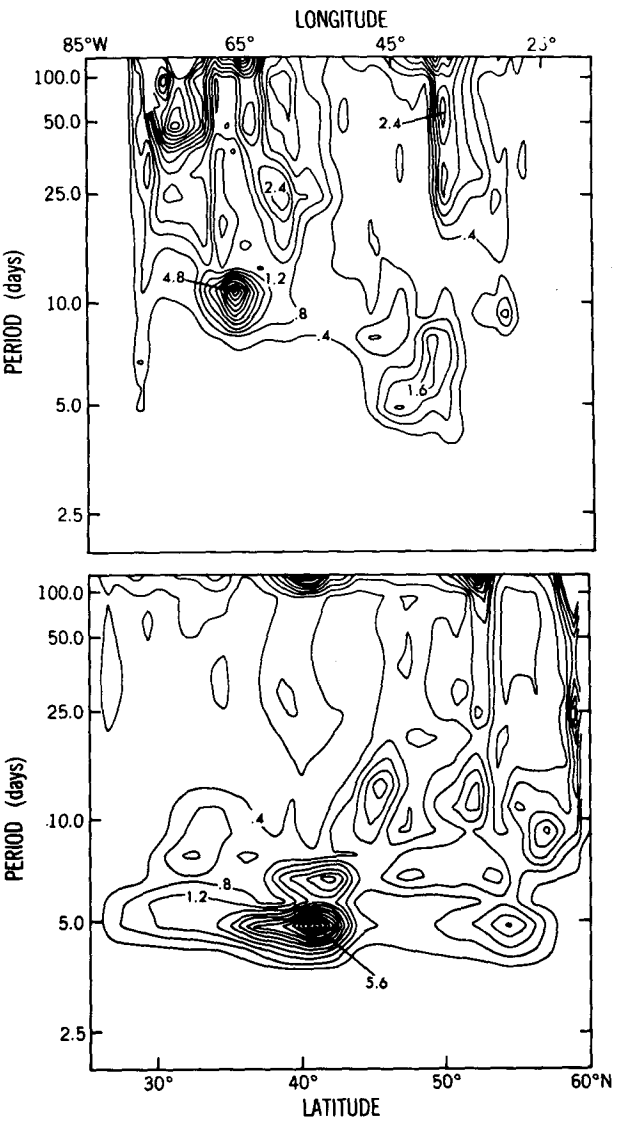

FIG. 10. Isopleths of energy density as a function of frequency along the meridian, and latitude circle, shown in Fig. 9a as dotted lines. Values are in units of $10^{12}(\text{cm}^2\ \text{s}^{-1})^2/\text{cpd}^{-1}$ and isopleths are at intervals of 0.4 of these units.

5. Discussion of oceanic measurements

Our results should be relevant to the barotropic mode in the oceans. Strictly speaking this requires a sufficient number of measurements in the vertical for determination of the veritical integral (over the entire depth of the ocean) of the horizontal velocity components. Alternatively, if the motion is highly coherent over considerable distances in the vertical, especially in the deep ocean, then measurements at one point may be representative of the barotropic mode. Measurements at Site D (39°N, 70°W) show that the motion at depths of 1000 and 2000 m are highly coherent (Thompson, 1977). Let us assume that the observed motion is representative of the barotropic mode and proceed to see whether any of the properties of this motion is explained by the results of our model.

Fig. 11 shows the kinetic energy spectra of the measurements at Site D. There are three frequency ranges with distinct properties. Thompson (1977) analyzed fluctuations with periods between a week and a month and showed that they correspond to topographic Rossby waves; at periods less than a week the spectrum is "red" and has a slope of at least −3; at periods longer than a month the spectrum is essentially "white." Fig. 12 shows the cross spectrum of zonal velocity measurements made at 39°9′N, 70°W and 39°9′N, 70°30′W. The data were taken over a 237-period starting April 1974 at a depth of 1000 m. As the bottom contours near Site D are

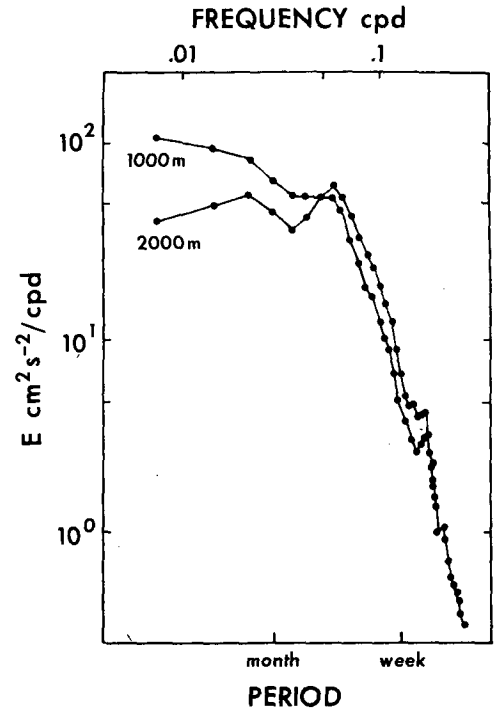

FIG. 11. Kinetic energy spectra as measured at Site D at depths of 1000 and 2000 m (after Thompson, 1977).

roughly from east to west, the water being shallower toward the north, the planetary and topographic definition of west are identical. Fig. 12 shows westward phase propagation in the central frequency range, and the phases return to zero at longer periods. At higher frequencies the coherences are too low to determine the phase accurately. Most of the properties described above are consistent with our model.

The motion has no discernible seasonal cycle (Thompson, private communication, 1978), consistent with a linear oceanic response to a wind stress whose components do not have a seasonal cycle (even though the amplitude of the wind stress has a considerable seasonal cycle). We submit that the low-frequency fluctuations (with periods longer than a month) correspond to a Sverdrup flow on which are superimposed short Rossby waves and possibly forced baroclinic motion. The identification of a high-frequency forced-wave regime is less obvious. The spectra in Fig. 11 change their slope around 5 days, where that regime is likely to start. Considering the results of Section 3, one would expect to find coherence (though not perfect) between selected atmospheric and oceanic variables. We have calculated cross spectra between Thompson's data and wind stress derived from our weather maps for the appropriate time interval, but have not found any significant coherence between any variables in any frequency range. One obvious reason for the lack of coherence is that the scale of topography is smaller than the scale of forcing and may prevent a unique correspondence between current and wind components.

The pressure measurements on the ocean floor near the MODE central mooring (70°W, 28°N) give further information about the barotropic mode. A bottom pressure gauge effectively filters out baroclinic motion and isolates the barotropic mode, for the following reasons. Consider a motion in geostrophic balance so that

$$-\mathbf{f} \times (\mathbf{v}_{bc} + \mathbf{v}_{bt}) = \nabla(P_{bc} + P_{bt}), \qquad (24)$$

where the suffixes *bc* and *bt* denote baroclinic and barotropic, respectively. Now assume that $\mathbf{v}_{bc}$ and $\mathbf{v}_{bt}$ have the same order of magnitude. [The percentage of kinetic energy in the barotropic mode is estimated to be between 30 and 50% (see Richman *et al.*, 1977).] The horizontal scale of barotropic motion typically exceeds the scale of baroclinic motion by at least an order of magnitude. Hence for ∇P_{bc} in (24) to be comparable to ∇P_{bt} it is necessary that P_{bt} exceed P_{bc} by an order of magnitude. Hence an instrument that measures the total pressure $P_{bc} + P_{bt}$ will in effect measure P_{bt} only. (This argument is not valid in regions of rough topography where the horizontal scale of barotropic motion may be small.)

Brown *et al.* (1975) describe bottom pressure gauge measurements over a four-month period in the area of the MODE experiment. Within the MODE area (over a 200 km distance) fluctuations are in phase and highly coherent. Fluctuations in the MODE area are also coherent (over a 700 km distance) with

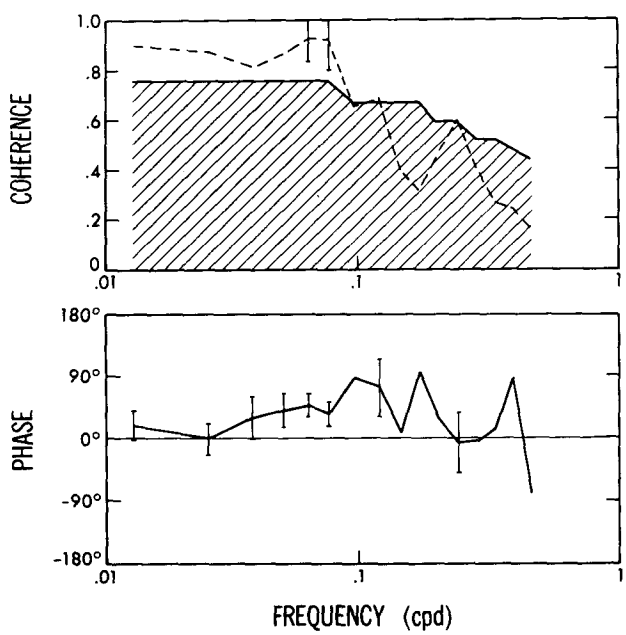

FIG. 12. Cross spectra of the zonal velocity components measured at two points separated in the east-west direction near Site D. Positive phase corresponds to westward phase propagation. (The data were kindly provided by J. Luyten.)

Bermuda subsurface pressure which implies that the oceanic pressure fluctuations have a large horizontal scale. It also indicates the success with which bottom pressure gages isolate the barotropic mode.

The local coherence between atmospheric and bottom ocean pressure is only marginally significant. Brown *et al.* (1975) infer from this that the cause of the bottom pressure fluctuations is probably not the local atmospheric forcing. They suggest that it is the barotropic response to a variable wind stress on the subtropical gyre; Rhines (1977) interprets these measurements as evidence of barotropic Rossby waves. On the other hand, our results show that in the Rossby wave range there should be absolutely no coherence between oceanic and atmospheric variables. Another puzzling feature of the measurements by Brown *et al.* (1975) is that in spite of the local coherence between oceanic and atmospheric pressure, the phase differences show propagation from Bermuda to the MODE area (i.e., with a westward component) in the ocean, but propagation in the opposite direction in the atmosphere.

Can our idealized model account for this apparent inconsistency? If we assume that the observed local coherence is real [and the chances that it is spurious are only 5% according to the statistics by Brown *et al.* (1975)], then the only way out seems to conclude that the bottom pressure P is a superposition of both a forced part P_f, and a Rossby wave part P_w, where $P = P_f + P_w$. Assuming that the forced part is uncorrelated with P_w and partly correlated with the atmospheric pressure P_a, then the coherence between oceanic and atmospheric pressure is found to be

$$\gamma_{PP_a} = \gamma_{P_fP_a}[\langle P_f^2\rangle/\langle P_f^2 + P_w^2\rangle]^{1/2}. \qquad (25)$$

For the horizontal phase difference $\Delta\phi$ in the ocean one finds, for small separation $\mathbf{r}$,

$$\Delta\phi = \frac{\langle P_f^2\rangle \mathbf{k}_f\cdot\mathbf{r} + \langle P_w^2\rangle \mathbf{k}_w\cdot\mathbf{r}}{\langle P_f^2\rangle + \langle P_w^2\rangle}, \qquad (26)$$

where $\mathbf{k}_f$ and $\mathbf{k}_w$ are the dominant wavenumbers of forced and wave constituent, respectively.

Now if $\gamma_{P_fP_a} \approx 0.8$ (cf. the high-frequency part of Fig. 7), and if we assume that forced and wave component have the same amplitude, $\langle P_f^2\rangle \approx \langle P_f^2\rangle$, then Eq. (25) predicts $\gamma_{PP_a} \approx 0.57$ which is close to the values reported by Brown *et al.* (1975). From (26) we infer that in the bottom pressure records the westward propagation will dominate if $k_w > k_f$, i.e., if the waves are of smaller scale than the cyclones. We therefore conclude that the pressure fluctuations observed by Brown *et al.* (1975) correspond to a superposition of locally forced waves (with eastward phase propagation) and non-locally generated planetary waves (with westward phase propagation). If the barotropic velocity fluctuations were also known, then it would be possible to infer spatial characteristics from the simultaneous measurements of velocity and pressure at *one point* (see Willebrand, 1978). Richman *et al.* (1977) estimated the barotropic velocities from the MODE central mooring but they are uncorrelated with the bottom pressure fluctuations. The mooring had three current meters only, too few for an accurate estimate of the barotropic component.

Further evidence for atmospheric generation of variable currents has come from current meter observations near the Iceland-Faeroe ridge. Meincke (1976) found that a strong event in the bottom current records coincided with the passage of a cyclone over that area. Meincke and Kvinge (1978) reported that coherences between bottom currents and atmospheric pressure differences marginally exceeded the significance level around a period of four days.

On the low-frequency side of the spectrum, Greisman and Aagaard (1979) observed that monthly variations of the total transport in the west Spitsbergen Current were related to fluctuations in the wind stress curl, although their data were insufficient to test the Sverdrup relations (22) and (23), respectively, quantitatively. They also found that the transport variations occurred almost exclusively in the barotropic flow component.

6. Summary

The direct generation of variable oceanic currents by large-scale atmospheric disturbances has been reinvestigated. In order to obtain results useful for the interpretation of oceanic current measurements, we describe observable patterns of atmospherically induced motion, rather than the dynamics of a single forcing event. The starting point of our discussion is the stochastic nature of atmospheric fluctuations, which have a local correlation time of only a few days. As a consequence of this limited local predictability, the energy spectra of atmospheric variables remain flat (white) at periods longer than the synoptic time scale. At the same time, the strong horizontal anisotropy in the atmosphere (with dominant eastward propagation of distrubances) is limited to the synoptic time scales, and fades away at lower frequencies. The oceanic response is weighted heavily toward longer time scales, so that an atmospheric forcing model which includes in a deterministic way only the dominant (cyclonic) variability of the atmosphere, is totally inadequate.

We have used variable wind stress fields as derived from synoptic weather maps to simulate the atmospheric forcing function as realistically as possible. Due to the absence of small-scale fluctuations in the weather maps, the induced oceanic response was found to be perfectly barotropic at all periods between a day and six months. Hence, in that period range Ekman pumping *cannot* contribute to changes in the heat content of the upper layer of the ocean. This conclusion depends only on the scale

of the forcing function, not on the forcing mechanism. It also applies to forcing by variable air pressure (which is generally unimportant except at the highest frequencies) and to thermal forcing which probably is effective only at lower (annual?) frequencies, [cf. Magaard (1977); Frankignoul and Müller (1980)].

From the barotropic vorticity equation for a flat-bottom ocean we infer that the stochastically forced response is characterized by three distinct frequency ranges:

1) At periods between 10 and 30 days the response is primarily in the form of planetary waves so that westward phase propagation is prominent. Only at a few discrete frequencies that correspond to resonant basin modes does friction determine the amplitude of these waves. In this free-wave regime there is no local coherence between oceanic and atmospheric fluctuations.

2) At periods between 1 and 10 days the response is no longer wavelike but is locally forced. Kinetic energy frequency spectra fall off rapidly with increasing frequency. Spectral slopes are between -2 and -4. This linear explanation for the shape of the observed spectrum in the frequency range of the energy "gap" is an alternative to the nonlinear one in terms of two-dimensional turbulent cascades which produce a ω^{-3} spectrum if a frozen turbulence assumption is made. In the forced wave band there can be an imperfect correlation between atmospheric and subsurface pressure, and between wind stress components and the corresponding current components. But inhomogeneities of the wind field can destroy these correlations.

3) At periods longer than a month the motion corresponds principally to a time-dependent Sverdrup balance. Current spectra are white and the zonal flow is more energetic than the meridional flow. The expected correlation between curl τ and the meridional velocity component can be destroyed by short Rossby waves even when their energy levels are low.

The results of a nonlinear numerical model that is forced with realistic winds confirm the above conclusions. Contrary to the results of earlier investigations, the rectifying effects of nonlinearities do not produce a significant mean circulation because the Rossby number of the flow is too small, and because of the random character of the wind-induced fluctuations. Haidvogel and Rhines (private communication, 1979) come to similar conclusions on the basis of independent numerical calculations. The fluctuating currents typically have amplitudes of a few centimeters per second and are most intense near the western boundary. Transport fluctuations of the western boundary layer can be as large as 20–30 Sv and are correlated with the net Sverdrup transport across the circle of latitude under consideration.

The configuration of coastlines does not influence the fluctuations very much but bottom topography alters the flow field significantly. The three distinct frequency bands will exist and frequency spectra have the same general shape as before but the free waves are now topographic rather than planetary Rossby waves. This leads to the possibility of trapping around certain topographic features and hence considerable horizontal inhomogeneities. Correlations between oceanic and atmospheric variables, which are found in flat-bottom models, can disappear when inhomogeneities of the bottom topography are taken into account.

Processes not included in our models can only further reduce the coherence between oceanic and atmospheric variables. A lack of correlations in reality does not therefore indicate a lack of causal relations—correlations are absent even in idealized models—but is indicative of the wavelike response of the ocean, of the broadband stochastic nature of atmospheric fluctuations, and of spatial inhomogeneities in the topography of the ocean floor.

The measurements of Brown *et al.* (1975) show that (small but statistically significant) correlations between oceanic and atmospheric variables can nonetheless be found in reality. [In Section 5 we point out that the instruments Brown *et al.* (1975) used, bottom pressure gauges, conveniently isolate the barotropic component of the flow and enhance the likelihood of finding correlation.]

How do we determine to what extent observed variability is atmospherically forced if it is difficult to establish correlations between oceanic and atmospheric fluctuations? We propose that the atmospherically induced barotropic motion be regarded as "background noise." This noise is typically of the order of a few centimeters per second and has a spectrum with a certain shape: red, with a slope between -2 and -4, at periods between a day and a week, and white at periods longer than a month. At periods between a week and a month westward phase propagation is most pronounced. If fluctuations observed in a certain region conform to this description, then we conclude that variability there is primarily atmospherically forced. An example of such a region is the neighborhood of Site D north of the Gulf Stream where the fluctuations have a large vertical coherence, and have energy levels and a spectral shape that closely corresponds to that of our background noise (Thompson 1977). (We have pointed out in Section 3d that the linear response to the observed atmospheric disturbances has no seasonal cycle. Current fluctuations at Site D do not have a seasonal cycle either.) We therefore propose that oceanic variability at Site D is primarily atmospherically forced.

At the MODE central mooring (Richman *et al.*, 1977) fluctuations have a small vertical coherence scale and have a spectrum that is red at periods

between 1 and 200 days. We conclude that variability there is not primarily forced by the atmosphere but must have an additional energy source. The measurements of Brown *et al.* (1975) suggest that the relatively small barotropic component of the flow could still be atmospherically induced.

The main deficiency of our synoptic forcing field is the absence of small-scale variability. The objective analysis scheme used to construct synoptic weather maps from observations smooths out fluctuations with a scale < 1000 km. As demonstrated in Section 2, the oceanic response changes qualitatively at scales of O(100 km). Frankignoul and Muller (1979) have estimated the response to a forcing field that includes small scales. They essentially extrapolated wavenumber spectra (the well-known k^{-3} kinetic energy spectrum, for example) toward high wavenumbers. They conclude that small-scale forcing could generate a significant amount of baroclinic motion which might account for observed mesoscale eddies in the ocean. At this stage, more information is necessary about the structure of the small-scale atmospheric disturbances to asses their importance.

Acknowledgments. We thank Dr. Jim Luyten for providing the current meter data discussed in Section 5. The expert technical assistance of Mr. P. Tunison and Ms. D. Raasch during manuscript preparation is gratefully acknowledged. This work has been supported through Geophysical Fluid Dynamics Laboratory/NOAA Grant 04-7-022-44017. One of us (J.W.) has been partially supported by the Deutsche Forschungsgemeinschaft.

REFERENCES

Bell, T. H., Jr., 1975: Statistical features of sea-floor topography. *Deep-Sea Res.*, **22**, 883–892.

Blumberg, A. F., 1977: Numerical tidal model of Chesapeake Bay. *J. Hydraulics Div., Proc. ASCE*, **103**, No. HY 1, 1–10.

Bretherton, F. P., and D. B. Haidvogel, 1976: Two-dimensional turbulence above topography. *J. Fluid Mech.*, **78**, 129–154.

Brown, W., W. Munk, F. Snodgrass, H. Mofjeld and B. Zetler, 1975: MODE bottom experiment. *J. Phys. Oceanogr.*, **5**, 75–85.

Firing, E., and R. C. Beardsley, 1976: The behavior of a barotropic eddy on a β-plane. *J. Phys. Oceanogr.*, **6**, 57–65.

Frankignoul, C., and P. Müller, 1979: Quasi-geostrophic response of an infinite β-plane ocean to stochastic forcing by the atmosphere. *J. Phys. Oceanogr.*, **9**, 104–127.

——, and ——, 1979: On the generation of geostrophic eddies by surface buoyancy flux. *J. Phys. Oceanogr.*, **9**, 1207–1213.

Garret, C. J. R., and W. H. Munk, 1972: Space-time scales of internal waves. *Geophys. Fluid Dyn.*, **2**, 225–264.

Gates, W. L., 1968: A numerical study of transient Rossby waves in a wind-driven homogeneous ocean. *J. Atmos. Sci.*, **25**, 3–22.

Greisman, Paul, and Knut Aagaard, 1979: Seasonal variability of the West Spitsbergen Current. *Ocean Modelling*, No. 19 (unpublished ms).

Harrison, D. E., 1979: On the equilibrium linear basin response to fluctuating winds and mesoscale motions in the ocean. *J. Geophys. Res.*, **84**, 1221–1224.

Herring, J. R., 1977: On the statistical theory of two-dimensional topographic turbulence. *J. Atmos. Sci.*, **34**, 1731–1750.

Holloway, Greg, 1978: A spectral theory of nonlinear barotropic motion above irregular topography. *J. Phys. Oceanogr.*, **8**, 414–427.

Leetma, A., 1978: Fluctuating winds: an energy source for mesoscale motions. *J. Geophys. Res.*, **83**, 427–430.

Lighthill, M. J., 1969: Dynamic response of the Indian ocean to onset of the southwest monsoon. *Phil. Trans. Roy. Soc. London*, **A265**, 45–92.

Longuet-Higgins, M. S., 1965: The response of a stratified ocean to stationary or moving wind-systems. *Deep-Sea Res.*, **12**, 923–973.

Magaard, Lorenz, 1977: On the generation of baroclinic Rossby waves in the ocean by meteorological forces. *J. Phys. Oceanogr.*, **7**, 359–364.

McWilliams, J. C., 1974: Forced transient flow and small scale topography. *Geophys. Fluid Dyn.*, **6**, 49–79.

Meincke, J., 1976: Coupling between bottom currents and weather pattern on the Iceland-Faroe ridge. Int. Council for Exploration of the Sea, C.M. 1976/C:30 (unpublished ms).

——, and T. Kvinge, 1978: On the atmospheric forcing of overflow events. Int. Council for Exploration of the Sea, C.M. 1978/C:9 (unpublished ms).

Müller, Peter, 1978: On the parameterization of eddy-mean flow interaction in the ocean. *Dyn. Atmos. Oceans*, **2**, 383–408.

Odulo, A. B., and E. N. Pelinovsky, 1978: Rossby wave attenuation above a rough bottom. *Polymode News*, No. 53 (unpublished ms).

Pedlosky, J., 1965a: A study of time-dependent ocean circulation. *J. Atmos. Sci.*, **22**, 267–272.

——, 1965b: A note on the western intensification of the oceanic circulation. *J. Mar. Res.*, **23**, 207–209.

Philander, S. G. H., 1978: Forced oceanic waves. *Rev. Geophys. Space Phys.*, **16**, 15–46.

Phillips, N. A., 1966: Large-scale eddy motion in the western Atlantic. *J. Geophys. Res.*, **71**, 3883–3891.

Rhines, P. B., 1977: The dynamics of unsteady currents. *The Sea*, Vol. 6, Wiley, 189–318.

——, and F. P. Bretherton, 1973: Topographic Rossby waves in a rough-bottomed ocean. *J. Fluid Mech.*, **61**, 583–607.

Richman, J. G., C. Wunsch and N. G. Hogg, 1977: Space and time scales of mesoscale motion in the western North Atlantic. *Rev. Geophys. Space Phys.*, **15**, 385–420.

Robinson, A. R., 1977: Mesoscale eddies. *Proc. JOC/SCOR Joint Study Conference on General Circulation Models and their Relation to Climate*. WMO/ICSU, Geneva, 1–30.

Semtner, A. J., Jr., and W. R. Holland, 1978: Intercomparison of quasi-geostrophic simulations of the western North Atlantic circulation with primitive equation results. *J. Phys. Oceanogr.*, **8**, 735–754.

Taylor, P. T., L. A. Banchero, C. M. Gordon and D. Greenewalt, 1977: Bottom water movement and the distribution of acoustically transparent sediment around the Gilliss Seamount, New England Seamount chain. *Trans. Amer. Geophys. Union*, **58**, 405.

Thompson, R. O. R. Y., 1977: Observations of Rossby waves near Site D. *Progr. Oceanogr.*, **7**, 135–162.

Thomson, R. E., 1975: The propagation of planetary waves over a random topography. *J. Fluid Mech.*, **70**, 267–285.

Veronis, George, 1970: Effect of fluctuating winds on ocean circulation. *Deep-Sea Res.*, **17**, 421–434.

——, and Henry Stommel, 1956: The action of variable wind stresses on a stratified ocean. *J. Mar. Res.*, **15**, 43–75.

Whitehead, J. A., 1975: Mean flow generated by circulation on a β-plane: An analogy with the moving flame experiment. *Tellus*, **28**, 358–364.

Willebrand, Jürgen, 1978: Temporal and spatial scales of the wind field over North Pacific and North Atlantic. *J. Phys. Oceanogr.*, **8**, 1080–1094.